Angewandte Chemie

DOI: 10.1002/ange.201306871

Multifunctional 2D Nanohybrids | Hot Paper

Polyaniline-Coupled Multifunctional 2D Metal Oxide/Hydroxide Graphene Nanohybrids**

Shuang Li, Dongqing Wu, Chong Cheng, Jinzuan Wang, Fan Zhang, Yuezeng Su, and Xinliang Feng**

Owing to their unique properties compared with conventional bulk analogues, two-dimensional (2D) nanomaterials, having nano-scale thickness and infinite length, are attracting increasing attention for their potential application in the fields of electronics, sensing, energy storage, and conversion.[1–8] In particular, transition-metal chalcogenides[9–15] and metal oxide[16] nanosheets are highly promising functional 2D nanomaterials, however, their synthesis in a large scale remains a great challenge. Graphene, a 2D "aromatic" monolayer of carbon material having an ultralight weight, high surface area, and electric conductivity, has emerged as an ideal substrate for the growth and anchoring of functional nanomaterials, such as metal oxide/hydroxide nanoparticles (MO/MH NPs).[3,17–19] The strong coupling between MO/MH NPs and graphene in a confined 2D manner gives nanohybrids with unique structural features and synergistic physical and electrochemical properties derived from both counterparts.[20–23] Along this line, numerous 2D functional nanohybrids comprising MO/MH NPs and graphene have been successfully constructed.[24–27] Nevertheless, owing to the general incompatibility between graphene and inorganic NPs under synthetic conditions, the growth of MO/MH NPs on a graphene substrate with uniform morphology, controllable particle size, and enhanced coupling effects constitutes a highly desirable synthetic target.

Polyaniline (PANI) is a typical low-cost conducting polymer that can be readily shaped into multiform morphologies, such as fibers/tubes,[28,29] dots/shells,[30] and other oriented nanostructures.[31] Hydrothermal treatment has proven to be an excellent strategy for fabricating PANI NPs.[32] Therefore, given that the protonated nitrogen atoms in PANI can bind with metal ions and mediate their hydrolysis process during hydrothermal treatment, we imagined that graphene-supported PANI nanosheets can facilitate the growth of MO and MH nanocrystals, and thus give rise to ternary nanohybrid sheets with a uniform distribution of hybrid NPs.

Herein, we demonstrate an efficient and universal strategy for the controlled growth of MO/MH (such as Co_3O_4, Fe_2O_3, and $Ni(OH)_2$) NPs on graphene to construct unique 2D nanohybrids employing PANI as the coupling linker between the two components. These nanohybrids have a well-defined 2D morphology, confined MO/MH NPs within the PANI nanostructures, controllable particle size, and high specific surface areas. The fabricated ternary hybrids of graphene, PANI, and Co_3O_4 (G-PANI-Co_3O_4) with a particle size of 6 to 10 nm deliver excellent rate capability and cycle performance when used as electrode materials for supercapacitors. Further, thermal treatment of G-PANI-MOs/MHs under inert gas yields nitrogen-doped carbon nanosheets integrated with size-controlled metal NPs (GNC-M). For example, N-doped carbon nanosheets supported by 3 to 5 nm sized cobalt NPs (GNC-Co) are synthesized by pyrolysis of G-PANI-Co_3O_4. The GNC-Co nanohybrids exhibit outstanding catalytic behavior for the oxygen-reduction reaction (ORR).

The overall synthetic strategy of 2D ternary graphene, PANI, and MO/MH (G-PANI-MOs/MHs)-coupled nanohybrids is illustrated in Figure 1a. First, graphene oxide (GO) nanosheets were functionalized with polyaniline by in situ polymerization of aniline in a GO suspension, which led to the formation of GO-based polyaniline (GO-PANI) nanosheets after centrifugation. Second, at pH 7 the GO-PANI nanosheets were mixed with the corresponding metal salts as the precursors of MO/MH followed by hydrothermal treatment. During this process, PANI particles formed on the graphene surface, while MO/MH NPs grew simultaneously and were confined within the PANI nanostructures. Specifically, G-PANI-Co_3O_4 (1:3), G-PANI-Co_3O_4 (1:10), and G-PANI-Co_3O_4 (1:20) were fabricated using GO-PANI with different GO to aniline weight ratios of 1:3, 1:10, and 1:20 respectively, in the first step of the synthesis. By the similar means, graphene decorated with PANI-Fe_2O_3 hybrid NPs (G-PANI-Fe_2O_3 (1:10)) and PANI-$Ni(OH)_2$ hybrid NPs (G-PANI-$Ni(OH)_2$ (1:10)) were also synthesized. For comparison, GO-PANI nanosheets were directly treated under the same conditions with no addition of metal salts, the composites obtained were named G-PANI.

The morphology and microstructures of as-prepared GO-PANI, G-PANI, G-PANI-Co_3O_4 (1:3), G-PANI-Co_3O_4 (1:10),

---

[*] S. Li, Dr. Y. Su
School of Aeronautics and Astronautics
Shanghai Jiao Tong University
800 Dongchuan Road, Shanghai 200240 (P.R. China)
E-mail: yzsu@sjtu.edu.cn
Dr. D. Wu, C. Cheng, J. Wang, Dr. F. Zhang, Prof. X. Feng
School of Chemistry and Chemical Engineering
800 Dongchuan Road, Shanghai 200240 (P.R. China)
Prof. X. Feng
Max Planck Institute for Polymer Research
Ackermannweg 10, 55128 Mainz (Germany)
E-mail: feng@mpip-mainz.mpg.de

[**] This work was financially supported by the National Basic Research Program of China (973 Program: 012CB933404), the Natural Science Foundation of China (21174083 and 21102091), BASF, the Shanghai Pujiang Program (11J1405400), and an ERC grant 2DMATER.

Supporting information for this article is available on the WWW under http://dx.doi.org/10.1002/anie.201306871.

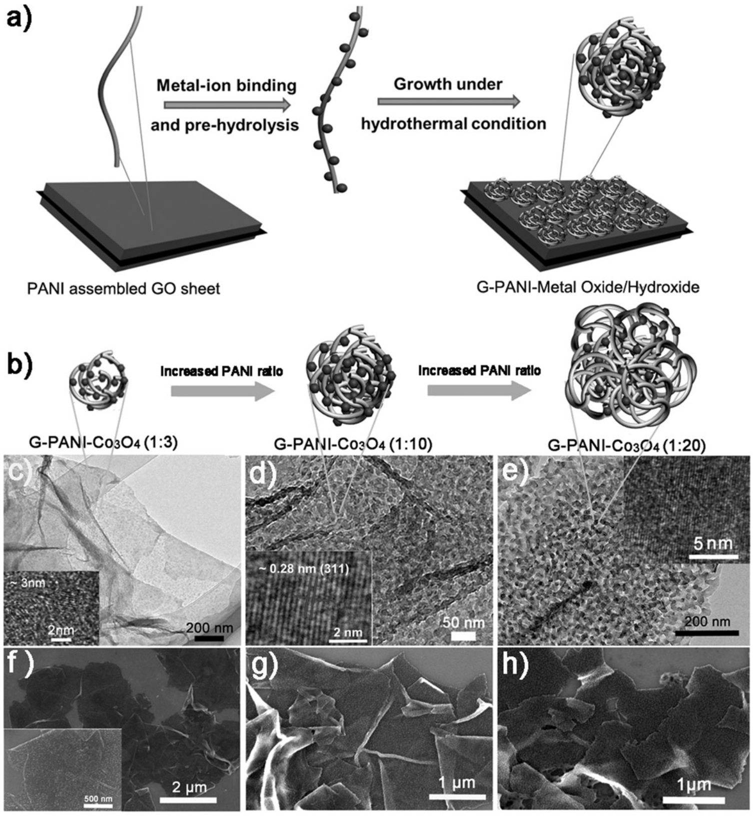

Figure 1. a) The overall synthetic procedure of G-PANI-MOs/MHs hybrids. b) The schematic illustration of PANI-Co_3O_4 hybrid particles. c)–e) The corresponding TEM images. f)–h) The corresponding SEM images of G-PANI-Co_3O_4 (1:3), G-PANI-Co_3O_4 (1:10), and G-PANI-Co_3O_4 (1:20) hybrids. Insets: HR-TEM images showing lattice spacings. The ratio is the ratio of graphene oxide:aniline in the initial synthetic step. Thus, the ratio of PANI is increased by increasing the ratio of aniline used initially.

and G-PANI-Co_3O_4 (1:20) were investigated by field-emission scanning electron microscopy (FE-SEM) and transmission electron microscopy (TEM), Figure 1 c–h. The TEM image of GO-PANI (Supporting Information, Figure S1) shows uniform 2D sheet morphology with a smooth surface. In contrast, after hydrothermal treatment, abundant small particles (ca. 5–15 nm) were formed on the graphene surface for G-PANI (Figure S1). This finding suggests that PANI readily assemble into small particles during the hydrothermal process. When cobalt salts are added in the hydrothermal treatment, sheets of the ternary hybrids should be formed. FE-SEM images reveal the ideal 2D sheet morphology of the nanohybrids with uniformly distributed PANI-Co_3O_4 hybrid NPs (Figure 1). For comparison, Co_3O_4 NPs directly grown on pristine GO without PANI were also examined (Figure S1). The particle size of Co_3O_4 ranged from 200 to 600 nm with irregular shapes, and it was difficult to identify any 2D sheet structure in the composites. TEM images further disclosed the successful growth of PANI-Co_3O_4 particles on the graphene surface for G-PANI-Co_3O_4. For example, uniformly distributed NPs with a size of 3–5 nm were formed on G-PANI-Co_3O_4 (1:3) (Figure 1 c). Interestingly, when the ratio of graphene to aniline was increased to 1:10 in the first step of the synthetic process, the particle size of PANI-Co_3O_4 increased to 6–10 nm (Figure 1 d); and for G-PANI-Co_3O_4 (1:20), the particle size of PANI-Co_3O_4 was approximately 15 nm (Figure 1 e). Thereby, this result strongly suggests that by adjusting the ratio of graphene to aniline, the size of PANI-Co_3O_4 hybrid particles can be well-controlled. Atomic force microscopy (AFM) measurements further revealed that the thickness of the G-PANI-Co_3O_4 (1:3), G-PANI-Co_3O_4 (1:10), and G-PANI-Co_3O_4 (1:20) sheet were approximately 26, 44, and 60 nm (Figure 2 a–c), with a surface roughness of approximately 3, 5, and 12 nm (Figure S3), respectively. This result matches well with the particle sizes measured by TEM.

The crystallinity of Co_3O_4 nanocrystals in G-PANI-Co_3O_4 hybrids was then investigated by high-resolution TEM (HR-TEM). Clear shell-lattice-fringes with d-spacing of 0.28 nm, corresponding to the (311) planes of Co_3O_4 can be seen in Figure 1 c–e. X-ray diffraction (XRD) patterns (Figure S4a) further revealed that all the peaks for G-PANI-Co_3O_4 (1:3), G-PANI-Co_3O_4 (1:10), and G-PANI-Co_3O_4 (1:20) could be assigned to the Co_3O_4 crystal (JCPDS no. 43-1003). Thermogravimetric analysis (TGA) showed that the weight content of Co_3O_4 in G-PANI-Co_3O_4 (1:3), G-PANI-Co_3O_4 (1:10), and G-PANI-Co_3O_4 (1:20) was 24, 26, and 13 %, respectively (Figure S4b). The low weight ratio of Co_3O_4 in G-PANI-Co_3O_4 (1:20) might be due to the overloaded and compacted PANI layer in the composites that only absorbed a limited amount of cobalt salts during the hydrothermal reaction. The specific surface areas of G-PANI-Co_3O_4 (1:3), G-PANI-Co_3O_4 (1:10), and G-PANI-Co_3O_4 (1:20) were calculated to be 84, 148, and 168 m^2g^{-1}, respectively, based on the Brunauer–Emmett–Teller (BET) method, (Figure S4c and d), which are higher than most reported Co_3O_4 nanosheet and mesoporous Co_3O_4 particles.[33–35]

Scanning TEM and elemental mapping analysis of G-PANI-Co_3O_4 (1:10) were performed to illustrate the distribution of carbon, nitrogen, cobalt, and oxygen components in the hybrids (Figure 2 d–i). Apparently, the carbon and nitrogen components were uniformly distributed in 2D nanosheets; in contrast, the cobalt and oxygen species were only identified within the nanometer-sized domains, which are nevertheless homogeneously distributed on the 2D nanosheets. These results imply that Co_3O_4 nanocrystals are fully confined within the shrunken PANI particles during the hydrothermal treatment and the three components (PANI, Co_3O_4, and graphene) are strongly coupled together in the nanohybrids.

The high surface area, thinness, good conductivity, and electrochemical activity of G-PANI-Co_3O_4 nanohybrids make them highly promising for application as electrode materials in supercapacitors. Cyclic voltammetry (CV) was used to evaluate the electrochemical behavior of G-PANI-Co_3O_4 (1:3), G-PANI-Co_3O_4 (1:10), and G-PANI-Co_3O_4 (1:20) electrodes in 6.0 M aqueous KOH electrolyte at a potential

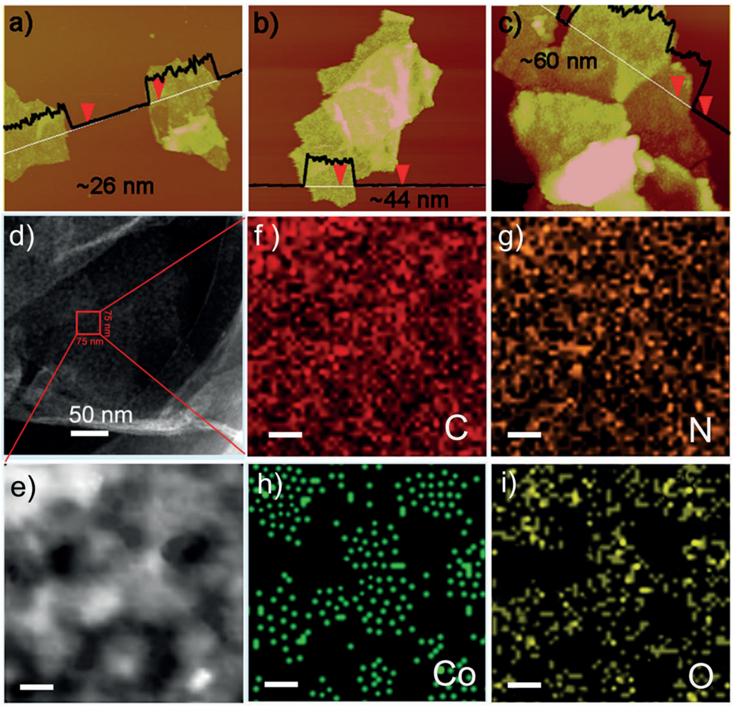

Figure 2. AFM images of a) G-PANI-Co_3O_4 (1:3), b) G-PANI-Co_3O_4 (1:10), and c) G-PANI-Co_3O_4 (1:20) nanosheets showing their thickness, d) and e) scanning TEM images of G-PANI-Co_3O_4 (1:10) and the corresponding elemental mapping images of f) C, g) N, h) Co, and i) O. The scale bars for (e)–(i) are 10 nm.

interval ranging from 0 to 0.4 V versus the Ag/AgCl electrode in a three-electrode system at a scan rate of 10 mV s^{-1} (Figure 3 a). All three curves showed similar redox current peaks corresponding to the reversible reactions of Co^{2+} to Co^{3+}. The specific capacitances of G-PANI-Co_3O_4 (1:3), G-PANI-Co_3O_4 (1:10), and G-PANI-Co_3O_4 (1:20) were calculated to be 713, 938, and 500 F/g, respectively (based on the whole hybrids). The prominent performance of G-PANI-Co_3O_4 (1:10) can be attributed to the optimal balance of specific surface area, particle size, and Co_3O_4 content. For comparison, we also examined G-PANI under the same conditions, which showed a capacitance of approximately 126 F/g (Figure S6). This result indicated that PANI can partly contribute to the capacitance, while its main function is to improve the conductivity of Co_3O_4 and enhance the coupling effects between graphene and Co_3O_4.

The capacitive behavior of G-PANI-Co_3O_4 (1:10) was further investigated by CV at various scan rates from 5 to 100 mV s^{-1} (Figure 3 b). Increasing the scan rate further enhanced the CV curve and redox peaks, indicating the excellent rate performance of the hybrids. It is striking to note that the capacitance of G-PANI-Co_3O_4 (1:10) was as high as 719 F/g at a scan rate of 100 mV s^{-1} (Figure 3 c). The charge-discharge behavior of G-PANI-Co_3O_4 (1:10) at different current densities is depicted in Figure 3 d. The specific capacitances were calculated to be approximately 1063, 1028, 952, 900, and 844 F/g (based on the whole hybrids) at current densities of 1, 2, 5, 10, and 20 A g^{-1}, respectively. The cycling stability of G-PANI-Co_3O_4 (1:10) against the charge–discharge cycles was investigated at a current density of 1 A/g (Figure S5). Remarkably, the specific capacitance of the electrode could be maintained at 1010 F/g (> 95 % capacitance retention) after 2500 cycles. To our knowledge, such electrochemical performance of G-PANI-Co_3O_4 (1:10) is superior to that reported in the literature for Co_3O_4/graphene,[36] Co_3O_4/carbon,[37] Co_3O_4/conducting polymer (such as polyaniline, polypyrrole),[38] and mesoporous Co_3O_4.[33–35]

To gain insight into the prominent electrochemical behavior of G-PANI-Co_3O_4 (1:10) electrode, AC impedance measurements were performed. Nyquist plots (Figure S7) show that the diameter of the semicircle of G-PANI-Co_3O_4 (1:10) electrode in the high medium frequency region is much smaller than G-Co_3O_4 electrode, suggesting that G-PANI-Co_3O_4 (1:10) electrode has lower contact and charge-transfer impedances. This result also validates that the

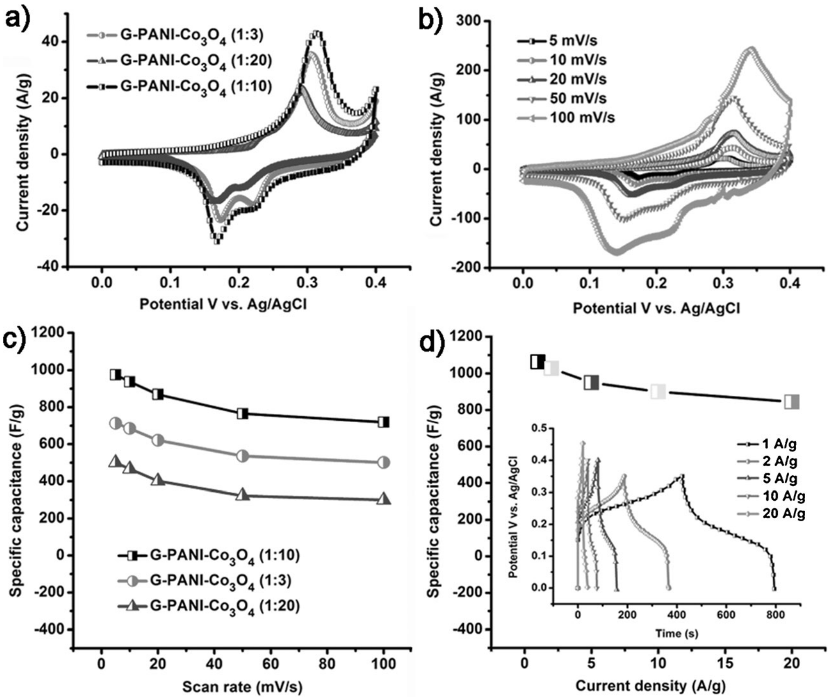

Figure 3. Electrochemical characterizations of G-PANI-Co_3O_4: a) CV curves of G-PANI-Co_3O_4 (1:3), G-PANI-Co_3O_4 (1:10), and G-PANI-Co_3O_4 (1:20) at a scan rate of 10 mV s^{-1}. b) CV curves of G-PANI-Co_3O_4 (1:10) at various scan rates. c) Specific capacitance of G-PANI-Co_3O_4 (1:3), G-PANI-Co_3O_4 (1:10), and G-PANI-Co_3O_4 (1:20) at various scan rates. d) Galvanostatic discharge curves of G-PANI-Co_3O_4 (1:10) at various discharge current densities and mean specific capacitance at various discharge current densities.

introduced PANI can improve the electrical conductivity of the overall electrode. Therefore, the superior electrochemical performance of G-PANI-Co_3O_4 (1:10) can be assigned to the synergistic effects of graphene, PANI, and Co_3O_4 associated with a unique 2D structure, this results in: 1) improvement of the structural stability and chemical resistance of Co_3O_4 during the electrochemical process through the strong coupling and interaction between the graphene, PANI, and Co_3O_4; 2) the increased electrolyte contact area and reduced diffusion distance for electrolytes and electrons as a result of the nanoscale thickness and high specific surface area of 2D hybrids; 3) the high electrical conductivity of the overall electrode and thus enhanced electron transport as a result of the combination of graphene and PANI; and 4) the additional capacity contributed by the PANI layer in 2D nanohybrids.

Our synthetic method can be further extended to build up other MO/MH NPs on graphene with well-controlled particle size and 2D morphology. To this end, we also successfully prepared G-PANI-Fe_2O_3 (1:10) (Figure S8) and G-PANI-$Ni(OH)_2$ (1:10) (Figure S9) nanohybrids with uniformly decorated PANI-Fe_2O_3 and PANI-$Ni(OH)_2$ hybrid NPs of approximately 5–10 nm. The BET surface areas of G-PANI-Fe_2O_3 (1:10) and G-PANI-$Ni(OH)_2$ (1:10) were calculated to be 168 and 166 $m^2 g^{-1}$, respectively. The loading amounts of Fe_2O_3 and $Ni(OH)_2$ measured by TGA (Figure S10) were 30 % and 21 %, respectively. As expected, G-PANI-$Ni(OH)_2$ (1:10) nanohybrids also displayed excellent electrochemical activity when used as the electrode materials for supercapacitors as a result of their thinness, high surface area, and strong coupling effects between different components. It delivered a capacitance of about 1100 F/g after 2000 cycles at a current density of 1 A/g (Figure S5), superior to the reported graphene/$Ni(OH)_2$ nanohybrids.[25]

Non-precious-metal catalysts based on nitrogen-doped carbon-supported non-precious-metal (Fe, Co) for ORR have attracted tremendous attention in the last few years.[39–41] The uncontrollable particle size of metal NPs during the synthesis is the current bottleneck of such catalysts. For instance, large cobalt particles generally decrease the specific surface area and active sites of the hybrids, thus weakening the ORR performance.[42,43] We subjected G-PANI-Co_3O_4 (1:10) to thermal treatment at 900 °C under nitrogen atmosphere for 2 h, which led to the formation of 2D nitrogen-doped carbon sheets integrated with size-controlled cobalt NPs (GNC-Co). The FE-SEM image (Figure 4 a) revealed that the cobalt NPs have a size of approximately 3–5 nm and were uniformly distributed on 2D sheets. The Co NPs are slightly smaller than the original PANI-Co_3O_4 hybrid NPs, which is attributed to the decomposition and carbonization of PANI during pyrolysis. This result highlights the successful confinement of cobalt nanoparticles by wrapping in PANI and subsequent high-temperature treatment. The HR-TEM image (Figure 4 c) clearly demonstrates the shell-lattice-fringes, corresponding to the (111) planes of cobalt. The crystallinity of cobalt NPs was further demonstrated by the XRD pattern with the characteristic diffraction peaks of (111), (200), and (220) peaks for cobalt (JCPDS No. 15-0806). The maintained 2D morphology confers the hybrids with a high specific surface area of approximately 280 $m^2 g^{-1}$ (Figure S11).

The electrocatalytic properties of the fabricated GNC-Co catalysts towards ORR were evaluated using the rotating ring-disk electrode (RRDE) technique in 0.1 M KOH at a rotation rate of 1600 rpm (catalyst-loading ca. 0.4 $mg\,cm^{-2}$). Steady-state ORR polarization curves indicated that GNC-Co showed excellent activity in terms of onset potential and half-wave potential (Figure 4 d). The onset potential difference between the GNC-Co and the Pt (20 wt. % Pt, BASF) catalyst was only 55 mV, and for half-wave potential it was only 15 mV, comparable to the best values reported for non-precious-metal catalysts.[44] The selectivity for the four-electron reduction of oxygen by GNC-Co was studied. The calculated value of the electron-transfer number can reach 3.95 at a potential of −0.1 V. Accelerated durability tests showed that after 2000 continuous potential cycles, the half-wave potential $E_{1/2}$ of GNC-Co exhibited a negative shift by only 11 mV (Figure 4 e).[44] The electrocatalytic activity of the GNC-Co catalyst in acidic media was examined in 0.5 M H_2SO_4 (catalyst loading ca. 0.2 $mg\,cm^{-2}$, Figure S12). The onset potential was approximately 0.45 V vs. Ag/AgCl and the current density reached 4.0 $mA\,cm^{-2}$. The electron-transfer number calculated from the RRDE was about 3.94 at

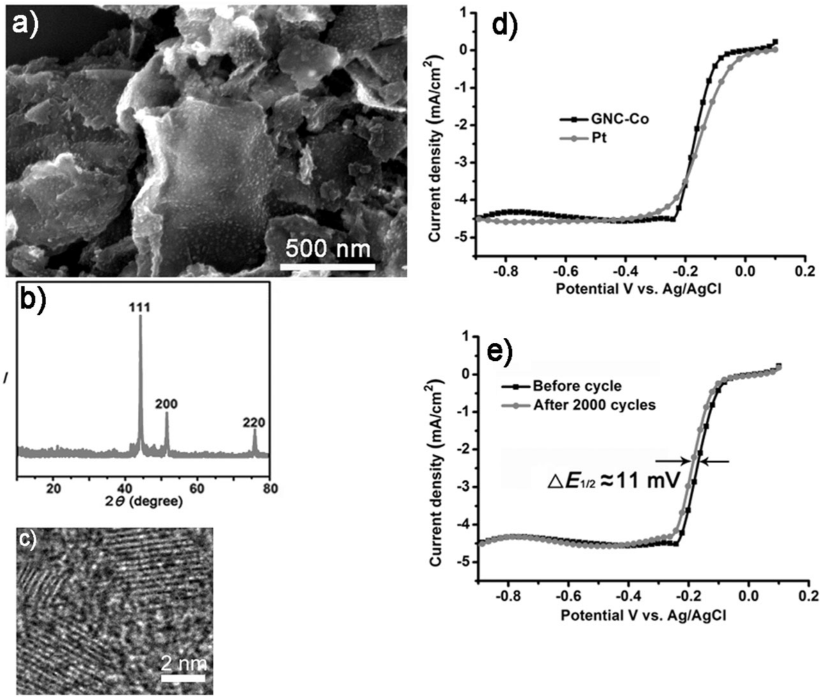

Figure 4. a) FE-SEM image, b) XRD pattern of the GNC-Co composite, c) HR-TEM image of GNC-Co, d) RDE curves of GNC-Co and Pt in 0.1 M KOH at a rotation rate of 1600 rpm, and e) RDE curves of GNC-Co before and after cycling.

0.45 V. Moreover, the durability of the GNC-Co catalyst was tested by CV (Figure S12), which showed almost no difference for the onset potential and peak potential after 2000 cycles compared with the 2nd cycle.

In summary, we developed a universal strategy for the controlled synthesis of strongly coupled nanosheets of graphene and MO/MH NPs by employing PANI as the coupling linker. These ternary nanohybrids have a well-defined 2D morphology, controllable particle size, nanoscaled thickness, and high specific surface area. These unique structural features give rise to the outstanding electrochemical performances of the hybrid nanosheets, thus facilitate their applications in electrochemical devices. We believe that the present synthetic method can be further extended to build up various 2D hybrids with promising applications across a broad range of catalysis, sensors, supercapacitors, and batteries.

Received: August 6, 2013

Keywords: graphene · nanoparticles · oxygen-reduction reaction · polyaniline · supercapacitors

---

[1] S. Yang, X. Feng, L. Wang, K. Tang, J. Maier, K. Müllen, *Angew. Chem.* **2010**, *122*, 4905; *Angew. Chem. Int. Ed.* **2010**, *49*, 4795.
[2] D. Wu, F. Zhang, H. Liang, X. Feng, *Chem. Soc. Rev.* **2012**, *41*, 6160.
[3] K. S. Novoselov, V. I. Falko, L. Colombo, P. R. Gellert, M. G. Schwab, K. Kim, *Nature* **2012**, *490*, 192.
[4] A. S. Aricò, P. Bruce, B. Scrosati, J. M. Tarascon, W. Van Schalkwijk, *Nat. Mater.* **2005**, *4*, 366.
[5] Y. Su, S. Li, D. Q. Wu, F. Zhang, H. Liang, P. Gao, C. Cheng, X. Feng, *Acs Nano* **2012**, *6*, 8349.
[6] X. Huang, Z. Zeng, Z. Fan, J. Liu, H. Zhang, *Adv. Mater.* **2012**, *24*, 5979.
[7] X. Huang, X. Qi, F. Boey, H. Zhang, *Chem. Soc. Rev.* **2012**, *41*, 666.
[8] X. Huang, Z. Yin, S. Wu, X. Qi, Q. He, Q. Zhang, Q. Yan, F. Boey, H. Zhang, *Small* **2011**, *7*, 1876.
[9] J. Seo, J. Jang, S. Park, C. Kim, B. Park, J. Cheon, *Adv. Mater.* **2008**, *20*, 4269.
[10] Y. Du, Z. Yin, J. Zhu, X. Huang, X. Wu, Z. Zeng, Q. Yan, H. Zhang, *Nat. Commun.* **2012**, *3*, 1177.
[11] H. Li, G. Lu, Y. Wang, Z. Yin, C. Cong, Q. He, L. Wang, F. Ding, T. Yu, H. Zhang, *Small* **2013**, *9*, 1974.
[12] Z. Zeng, Z. Yin, X. Huang, H. Li, Q. He, G. Lu, F. Boey, H. Zhang, *Angew. Chem.* **2011**, *123*, 11289; *Angew. Chem. Int. Ed.* **2011**, *50*, 11093.
[13] X. Huang, Z. Zeng, H. Zhang, *Chem. Soc. Rev.* **2013**, *42*, 1934.
[14] M. Chhowalla, H. S. Shin, G. Eda, L. J. Li, K. P. Loh, H. Zhang, *Nat. Chem.* **2013**, *5*, 263.
[15] X. Huang, Z. Zeng, S. Bao, M. Wang, X. Qi, Z. Fan, H. Zhang, *Nat. Commun.* **2013**, *4*, 1444.
[16] Y. Omomo, T. Sasaki, L. Wang, M. Watanabe, *J. Am. Chem. Soc.* **2003**, *125*, 3568.
[17] A. K. Geim, K. S. Novoselov, *Nat. Mater.* **2007**, *6*, 183.
[18] D. Wu, F. Zhang, P. Liu, X. Feng, *Chem. Eur. J.* **2011**, *17*, 10804.
[19] Z. S. Wu, Y. Sun, Y. Z. Tan, S. Yang, X. Feng, K. Müllen, *J. Am. Chem. Soc.* **2012**, *134*, 19532.
[20] M. D. Stoller, S. Park, Y. Zhu, J. An, R. S. Ruoff, *Nano Lett.* **2008**, *8*, 3498.
[21] L. Dai, *Acc. Chem. Res.* **2013**, *46*, 31.
[22] B. Luo, Y. Fang, B. Wang, J. Zhou, H. Song, L. Zhi, *Energy Environ. Sci.* **2012**, *5*, 5226.
[23] B. Luo, B. Wang, X. Li, Y. Jia, M. Liang, L. Zhi, *Adv. Mater.* **2012**, *24*, 3538.
[24] D. Wang, R. Kou, D. Choi, Z. Yang, Z. Nie, J. Li, L. V. Saraf, D. Hu, J. Zhang, G. L. Graff, J. Liu, M. A. Pope, I. A. Aksay, *ACS Nano* **2010**, *4*, 1587.
[25] H. Wang, H. S. Casalongue, Y. Liang, H. Dai, *J. Am. Chem. Soc.* **2010**, *132*, 7472.
[26] S. Yang, X. Feng, K. Müllen, *Adv. Mater.* **2011**, *23*, 3575.
[27] Q. Qu, S. Yang, X. Feng, *Adv. Mater.* **2011**, *23*, 5574.
[28] J. Huang, R. B. Kaner, *J. Am. Chem. Soc.* **2004**, *126*, 851.
[29] J. Huang, S. Virji, B. H. Weiller, R. B. Kaner, *J. Am. Chem. Soc.* **2003**, *125*, 314.
[30] Z. Zhang, J. Sui, L. Zhang, M. Wan, Y. Wei, L. Yu, *Adv. Mater.* **2005**, *17*, 2854.
[31] L. Liang, J. Liu, J. C. F. Windisch, G. J. Exarhos, Y. Lin, *Angew. Chem.* **2002**, *114*, 3817; *Angew. Chem. Int. Ed.* **2002**, *41*, 3665.
[32] L. J. Pan, L. Pu, Y. Shi, T. Sun, R. Zhang, Y. O. Zheng, *Adv. Funct. Mater.* **2006**, *16*, 1279.
[33] C. Yuan, L. Yang, L. Hou, L. Shen, X. Zhang, X. W. Lou, *Energy Environ. Sci.* **2012**, *5*, 7883.
[34] S. K. Meher, G. R. Rao, *J. Phys. Chem. C* **2011**, *115*, 15646.
[35] R. B. Rakhi, W. Chen, D. Cha, H. N. Alshareef, *Nano Lett.* **2012**, *12*, 2559.
[36] W. Zhou, J. Liu, T. Chen, K. S. Tan, X. Jia, Z. Luo, C. Cong, H. Yang, C. M. Li, T. Yu, *Phys. Chem. Chem. Phys.* **2011**, *13*, 14462.
[37] J. Zhi, S. Deng, Y. Zhang, Y. Wang, A. Hu, *J. Mater. Chem. A* **2013**, *1*, 3171.
[38] C. Zhou, Y. Zhang, Y. Li, J. Liu, *Nano Lett.* **2013**, *13*, 2078.
[39] G. Wu, K. L. More, C. M. Johnston, P. Zelenay, *Science* **2011**, *332*, 443.
[40] M. Lefèvre, E. Proietti, F. Jaouen, J. P. Dodelet, *Science* **2009**, *324*, 71.
[41] R. Bashyam, P. Zelenay, *Nature* **2006**, *443*, 63.
[42] U. I. Koslowski, I. Abs-Wurmbach, S. Fiechter, P. Bogdanoff, *J. Phys. Chem. C* **2008**, *112*, 15356.
[43] Z. Chen, D. Higgins, A. Yu, L. Zhang, J. Zhang, *Energy Environ. Sci.* **2011**, *4*, 3167.
[44] Y. Li, W. Zhou, H. Wang, L. Xie, Y. Liang, F. Wei, J. C. Idrobo, S. J. Pennycook, H. Dai, *Nat. Nanotechnol.* **2012**, *7*, 394.